

Scalable Transfer-Free Fabrication of MoS₂/SiO₂ Hybrid Nanophotonic Cavity Arrays with Quality Factors Exceeding 4000

Sebastian Hammer^{1,2}, Hans-Moritz Mangold^{1,2}, Ariana E. Nguyen³, Dominic Martinez-Ta³, Sahar Naghibi Alvillar³, Ludwig Bartels³, Hubert J. Krenner^{1,2,4,*}

¹ Lehrstuhl für Experimentalphysik 1 and Augsburg Centre for Innovative Technologies (ACIT), Universität Augsburg, Universitätsstraße 1, 86159 Augsburg, Germany

² Nanosystems Initiative Munich (NIM), Schellingstraße 4, 80799 München, Germany

³ Department of Chemistry and Materials Science & Engineering Program, University of California, Riverside, California 92521, USA

⁴ Center for Nanoscience (CeNS), Ludwig-Maximilians-Universität München, Geschwister-Scholl-Platz 1, 80539 München, Germany

* corresponding author: hubert.krenner@physik.uni-augsburg.de

ABSTRACT

We report the fully-scalable fabrication of a large array of hybrid molybdenum disulfide (MoS₂) - silicon dioxide (SiO₂) one-dimensional, free-standing photonic-crystal cavities capable of enhancement of the MoS₂ photoluminescence at the narrow cavity resonance. We demonstrate continuous tunability of the cavity resonance wavelength across the entire emission band of MoS₂ simply by variation of the photonic crystal periodicity. Device fabrication started by substrate-scale growth of MoS₂ using chemical vapor deposition (CVD) on non-birefringent thermal oxide on a silicon wafer; it was followed by lithographic fabrication of a photon crystal nanocavity array on the same substrate at more than 50% yield of functional devices. Our cavities exhibit three dominant modes with measured linewidths less than 0.2 nm, corresponding to quality factors exceeding 4000. All experimental findings are found to be in excellent agreement with finite difference time domain simulations.

MAIN TEXT

Monolayer transition metal dichalcogenides (TMDs) have recently attracted great interest in the field of photonics because of their distinctive optical and spin properties^{1–3}. In contrast to bulk TMD materials, which are indirect bandgap semiconductors, monolayer TMDs are highly optical active due to a direct bandgap ranging between 1 and 2 eV^{4,5}. In contrast to top-down fabrication methods like exfoliation^{5,6}, which yields single TMD flakes of high purity, but does not permit scalability or systematic control of flake thickness and size, chemical vapor deposition (CVD) generates large-scale TMD films of uniform layer thickness and excellent optical and electrical properties^{7,8}. Even continuous spatial tuning of the optical bandgap within composite layers of different TMDs has been realized^{9,10}.

The integration of optically active materials into photonic circuits, for example as light emitters or non-linear elements, requires efficient coupling of TMD excitons to optical fields. This can be dramatically enhanced by nanophotonic resonators. For instance, increased light extraction, signatures of Purcell enhanced emission, and even lasing were observed in systems of TMD monolayers transferred onto two-dimensional GaP-based photonic crystal cavities (PCCs)^{11–13} or whispering gallery microdisk resonators¹⁴. While these studies^{11–13} utilized exfoliation of a TMD layer and transfer onto the completed photonic crystal structure, large-

scale applications will require direct growth of homogeneous TMD films onto the substrate as an essentially processing step. Thermally grown SiO_2 is an excellent candidate substrate for hybrid TMD-PCC devices. It is the most established substrate for CVD growth of TMDs¹⁵ and an essential component of state-of-the-art silicon technology. Moreover, amorphous SiO_2 is non-birefringent and exhibits a large optical bandgap of ~ 9 eV. These properties allow SiO_2 to stand out over alternative materials, in particular the commonly-used indirect semiconductor GaP.

Results

Here we demonstrate a sequence of CVD growth of a monolayer MoS_2 film followed by fabrication of dozens of free-standing one-dimensional MoS_2 - SiO_2 PCCs on a single substrate without any transfer steps in a fully-scalable approach. Across a broad library of different PCCs fabricated in a single step on the same substrate, we achieve wide linear tunability of the photonic mode spectrum throughout the entire emission band of MoS_2 , simply by changing the periodicity of the photonic lattice. Both the tuning and the experimentally demonstrated quality (Q) factors $Q > 4000$ are confirmed at high fidelity by finite difference time domain (FDTD) simulations.

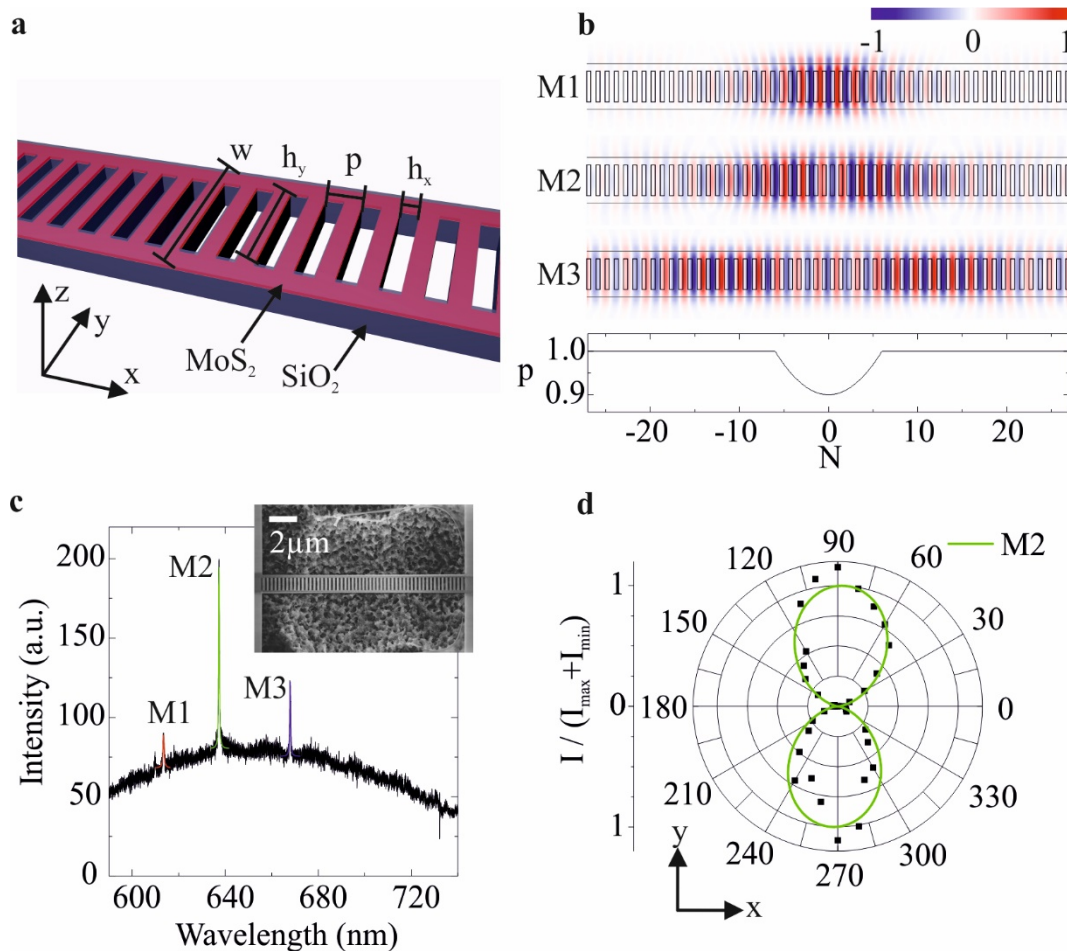


Figure 1. Structure, design and characterization – a. Layout of the ladder-type SiO_2 (purple) PCC covered on top by a CVD-grown MoS_2 monolayer (pink). b. Upper panels: E_y field distribution in the PCC (sketched) of the modes M1, M2, and M3 obtained from FDTD simulation. Lower panel: Period variation in the photonic crystal as a function of the hole position N along the ladder (counted from the center). The defined parabolic perturbation of the period forms the cavity. c. PL spectrum of a

typical PCC showing the broad MoS₂ emission decorated with three modes, M1, M2 and M3, which are fitted with Lorentzians (colored solid lines). Inset: SEM image of a fabricated PCC. d. Normalized and background corrected peak intensities of the M2 mode (symbols) as a function of the polarization angle and fit (green line) proving TE-polarization.

Due to the relatively low refractive index of SiO₂ (~ 1.46) a ladder-type PCC design is highly desirable¹⁶. The design used in this study is shown schematically in Figure 1a. This geometry allows for wavelength-scale confinement of the optical modes along the beam direction (x) and tight confinement in the perpendicular directions due to total internal reflection. Specifically, our design consists of a 200 nm thick, free-standing, MoS₂-SiO₂ nanobeam with etched rectangular holes at a base periodicity p . The beam width is $w = 4.75 p$ and the hole sizes are $h_x = 0.5 p$ in x -direction and $h_y = 0.7 w$ in y -direction. As shown in the bottom part of Figure 1b, the period of the first 7 holes in $\pm x$ -direction, counted from the ladder center, is modulated parabolically from $0.9 p$ to $1.0 p$. The upper panels of Figure 1b show the E_y field component of the three dominant TE-polarized localized modes, separately calculated by FDTD simulations. As expected¹⁷, the field distribution of the fundamental mode M1 shows a single antinode (maximum) in the center of the PCC. Modes M2 and M3 are the second- and third-order modes of this geometry, respectively.

Our fabrication process starts with CVD growth¹⁵ of MoS₂ directly on a 200 nm thermal oxide (SiO₂) layer of a Si substrate. After growth, we define the PCC pattern by electron beam lithography. The whole fabrication is described in detail in the methods section. A scanning electron micrograph of a typical free-standing PCC with a period of $p = 275$ nm is shown in the inset in Figure 1c. The total size of a single device, i.e. the area of the undercut region, is approximately $40 \mu\text{m} \times 40 \mu\text{m}$. In this work, we report on 32 devices fabricated within a rectangular area of $2 \text{ mm} \times 3.5 \text{ mm}$. Closer packing of these relatively large individual devices would in principle allow to integrate more than 5000 devices on a typical $1 \text{ cm} \times 1 \text{ cm}$ substrate. We note, that in our devices the active MoS₂ remains only within the rungs of the ladder, precisely the position of the antinodes of the cavity field. This unique feature ensures exclusive enhancement of the light-matter coupling. This is in strong contrast to hybrid devices fabricated by exfoliation and transfer of a 2D material on a prefabricated nanophotonic device^{11–13}.

Figure 1c shows the room temperature ($T = 300 \text{ K}$) micro-photoluminescence (μPL) spectrum (see methods section) of a typical PCC of period $p = 275$ nm. The broad background represents the PL emission of unstructured MoS₂⁴. In addition, the spectrum shows three sharp lines stemming from the expected localized photonic modes, M1, M2 and M3. Such cavity modes were detected from >50% of all studied PCCs. Lorentzian fits to these peaks (red, green and blue solid lines) reveal Q -factors of $Q_{M1} = 1000$ ($\Delta\lambda = 0.62 \text{ nm}$), $Q_{M2} = 1700$ ($\Delta\lambda = 0.38 \text{ nm}$) and $Q_{M3} = 1570$ ($\Delta\lambda = 0.42 \text{ nm}$), respectively, for this particular device. To confirm the TE-like character of these modes, we perform polarization dependent spectroscopy by placing a half-wave plate and a polarizer into the detection path of the μPL setup. Figure 1d shows the normalized and background corrected intensity of a M2 mode (symbols) as a function of the polarization angle α that is fitted with a \sin^2 function with a period fixed to 180 degrees (green solid line). The polarization direction transverse to the beam (i.e., in y -direction) confirms the TE-like mode character. To further quantify the polarized nature of the cavity modes, we evaluate the degree of polarization, $DoP = (I_{\text{max}} - I_{\text{min}}) / (I_{\text{max}} + I_{\text{min}})$, with I_{min} (I_{max}) being the minimum (maximum) intensity. From our data and fit, we obtain a value of $DoP = 1.000 \pm 0.013$ that is close to ideal.

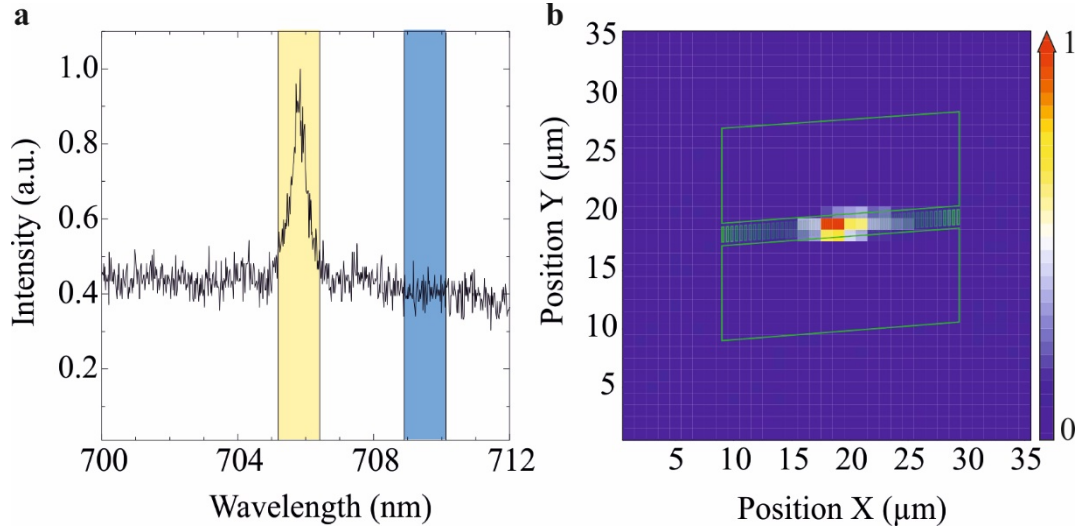


Figure 2. Spatial confinement – a. M1 mode of a cavity with period $p = 310$ nm. The integrated intensity in the spectral region of the cavity mode (left yellow-shaded region) is subtracted from the background (integrated counts of the right blue-shaded region). b. The resulting intensity distribution of the mode M1 shows strong spatial confinement at the center of the PCC (the green outline represents the ladder rungs and the RIE-etched regions defining the outer border of the ladder).

Scanning μ PL spectroscopy of a full structure is used to confirm the spatial localization and confinement of a PCC mode. For the data shown in Figure 2a, a total area of $35 \mu\text{m} \times 35 \mu\text{m}$ was scanned at $1 \mu\text{m}$ steps. At each position, a full PL spectrum of the M1 mode was recorded. Figure 2a shows the spectrum recorded at the center of the nanocavity at position $(x/y) = (19 \mu\text{m}/19 \mu\text{m})$. We quantify the enhancement of the M1 emission by integration of the PL emission in the wavelength range of the cavity resonance (marked by the yellow box in Figure 2a) and subtraction of the integrated intensity in a wavelength interval of identical width in close spectral proximity of the mode (marked by the blue box in Figure 2a) for background correction. Performing this procedure at every point of the μ PL scan, we are able to build a spatial emission enhancement map, which we normalize to its absolute maximum. Figure 2b shows this emission enhancement map. Superposition of the outline of the etched PCC structure reveals strong emission enhancement at the resonance wavelength of M1 directly in the center of the structure. This finding directly validates the tight spatial localization of the PCC mode.

The PCC resonance wavelengths can be tuned by variation of the crystal period. Figure 3a shows the emission spectra recorded from a series of PCCs with periods tuned from $p = 270$ nm to 325 nm in steps of $\Delta p = 5$ nm. The PCC modes exhibit a continuous shift to longer wavelengths as p increases. For short periods $p \leq 285$ nm, modes M1, M2 and M3, marked by red, green and blue arrows, respectively, overlap with the emission band of MoS₂. Starting at $p = 290$ nm (green spectrum), an additional mode M* (black arrow) appears at shorter wavelengths, which also exhibits TE-like character in polarization-dependent measurements. As p increases up to 325 nm, the entire mode spectrum of the PCC continuously shifts across the full MoS₂ emission band.

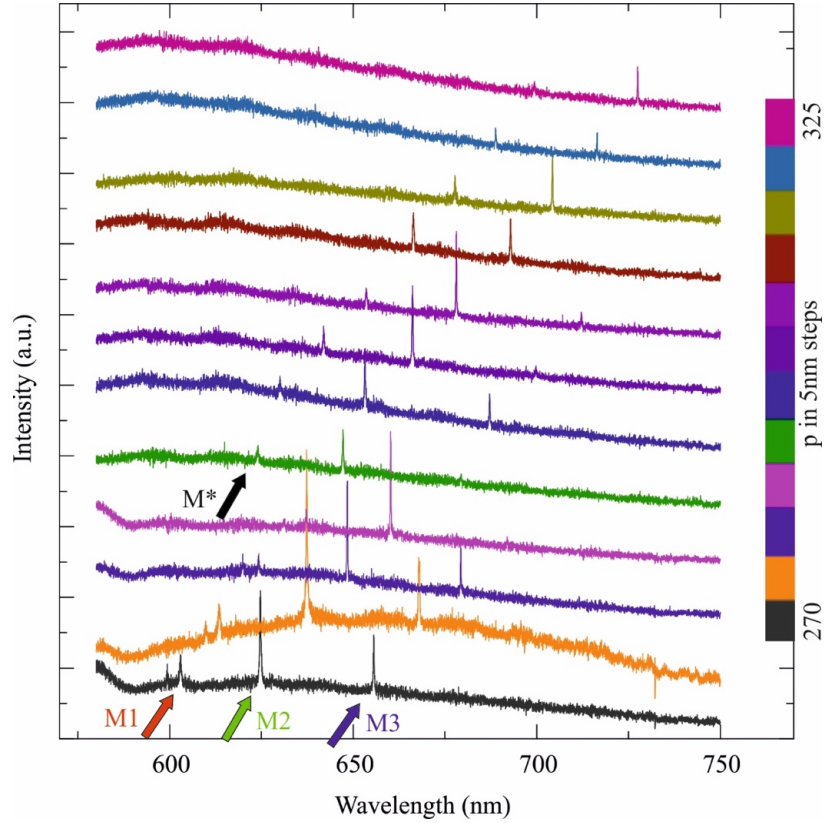


Figure 3. Geometric tuning – Spectra of PCCs with periods from 270 nm (bottom) to 325 nm (top). The red (green, blue) arrow marks the M1 (M2, M3) mode. The resonance wavelengths increase linearly with the period. PCCs with $p \geq 290$ nm show an additional mode M^* (marked by the black arrow).

We analyzed the spectra obtained on each of the PCC structures in detail and extracted both the resonance wavelengths and the Q -factors of the PCC modes. For reference, Figure 4a shows a typical PL spectrum of unstructured MoS_2 . A composite image of a subset of the array of PCC cavities fabricated on a single chip is shown in Figure 4b. Figures 4c and d aggregate the experimentally measured mode wavelengths and Q -factors as a function of the PCC periodicity, respectively. Experimental results are plotted as symbols with the symbol color matched to the mode assignment of Figure 3. The error bars indicate the standard deviation of the mean value obtained by fabrication of more than one PCC at a given periodicity.

Figure 4c reveals clear linear tuning behavior of the resonance wavelengths for all observed cavity modes¹⁶. Such linear tuning is precisely predicted by our FDTD simulations, which are detailed in the Methods section. The resonance wavelengths of M1 are calculated for SiO_2 thicknesses of $d = 200$ nm (the actual SiO_2 thickness) and $d = 300$ nm (to account for residual resist left on top of the PCC). The gray area in Figure 4c shows the area where M1 is expected according to the simulations. The measured spectral shift follows faithfully these calculations. Figure 4d shows the Q -factor analysis. The measured Q -factors are plotted as symbols using the same color-code as in Figures 3 and 4a. Most remarkably, we derive high $Q > 1000$ for almost all PCC modes resolved. However, our experimentally derived values are systematically lower than those observed by Gong and coworkers¹⁶, presumably due to the thinner membranes used in our samples and increased optical absorption loss of MoS_2 . Our measured Q -factors are in excellent agreement with those expected from FDTD modeling (grey shaded area).

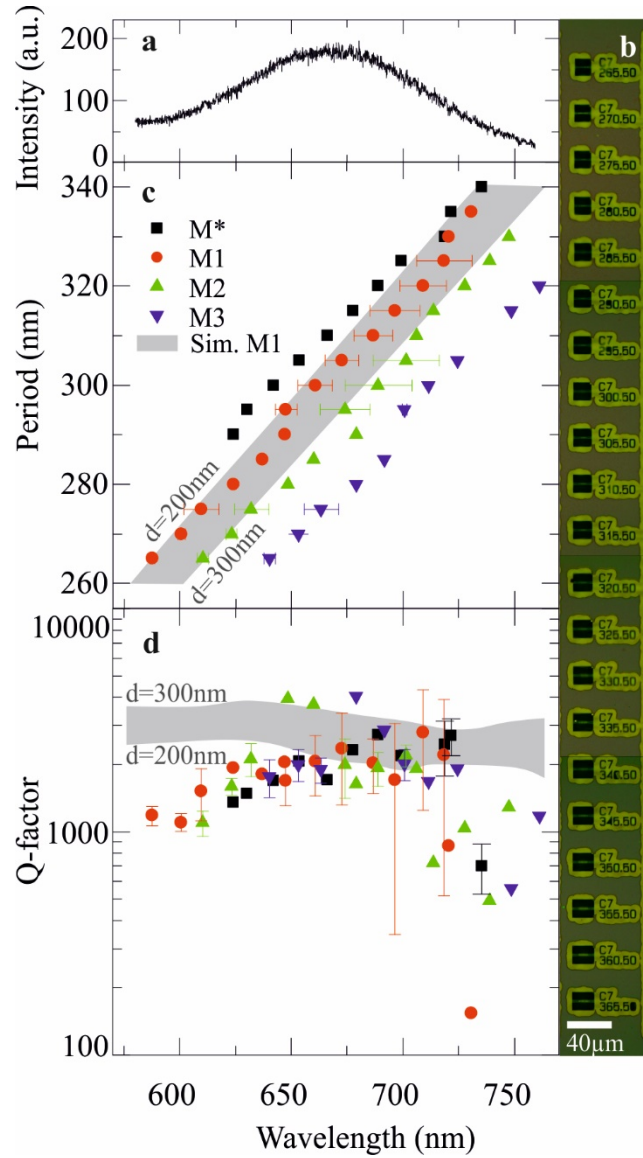


Figure 4. Tuning analysis and comparison to FDTD simulations – a. A typical MoS₂ PL spectrum. b. Optical microscope image of an array of 21 PCC devices fabricated on a continuous MoS₂ film. c. Geometric tuning analysis – The PCC periods within the set of cavities of Figure 3 are plotted as a function of the mode wavelength they support. M1, M2, M3 show excellent agreement with the linear tuning predicted by FDTD simulations for a SiO₂ thickness between $d = 200$ nm and 300 nm (grey shaded area). d. Experimentally observed Q-factor of the three dominant modes as a function of the wavelength the PCC supported. These values agree nicely with FDTD simulation results for M1 (grey shaded area).

Discussion

We designed and fabricated MoS₂-SiO₂ PCCs with Q -factors > 4000 . Simply by tuning the periodicity of the photonic lattice, we are able to tune the PCC mode spectrum across the entire PL emission peak of MoS₂. The modes exhibit strong TE polarization and are tightly confined in the cavity region. We show that geometrical tuning of the cavity resonances follows simulations closely and that the measured Q factors are in excellent agreement with our predictions for the ideal structure indicating the high quality throughout dozens of devices fabricated on the same chip – thus, highlighting the efficiency of our fabrication process. Our design can be natively transferred to other TMDs and TMD-based van der Waals

heterostructures¹⁸. In addition, their high Q -factor and strong field enhancement are ideally suited to enhance single-photon emission of quantum dot-like emission centers recently observed in the TMD WSe_2 ^{19,20}. The non-birefringent nature of SiO_2 is furthermore ideal for future applications in valleytronics. The cavity-enhanced light-matter interactions enable low power gating of the spin and valley degrees of freedom^{21,22} using a TMD coupled to an advanced non-polarizing cavity. Finally, the large localized electric fields in the cavity have the potential to offer access to non-linear optical effects such as second harmonic generation. In contrast to a recent report by Fryett and coworkers who used silicon cavities and an exfoliated TMD²³, the large optical bandgap of SiO_2 eliminates absorption losses of the visible/near-infrared photoluminescence of many TMDs. Our fully scalable approach is ideally suited for large-scale nanophotonic circuits²⁴ built from a toolbox of functional design elements²⁵. In such circuits the large-area CVD TMD layer will offer multiple functionalities as an optical emitter or a non-linear optical medium^{26,27} and a channel layer for associate drive electronics²⁸. In particular, simply by adding electrical contacts, the TMD layer can be transformed to an on-chip photodetector^{29,30} or a LED^{31–33}.

METHODS

CVD growth of MoS_2 :

Monolayer MoS_2 is grown onto the SiO_2/Si substrate via CVD utilizing elemental sulfur and MoO_3 powder as precursors¹⁵. Alumina boats containing the precursors are placed at different positions in a quartz process tube. A molybdenum mesh resting on the edge of the MoO_3 -containing boat is used to support the substrate. The furnace with the process tube is gradually heated up to 650–700°C. A continuous flow of N_2 gas is utilized to transfer sulfur vapor from the boat closer to the furnace edge to the growth substrate near the furnace center. The substrate is held at the indicated temperature for ~10 min for monolayer MoS_2 formation and then cooled-down gradually.

Lithographic Device Fabrication: The PCC pattern is written by electron beam lithography into 380 nm thick layer of spin-coated ZEP-520A resist. After development, this pattern is transferred into the $\text{MoS}_2\text{-SiO}_2$ layer by inductively coupled plasma reactive ion etching (ICP-RIE) using a $\text{CHF}_3:\text{O}_2$ chemistry (40sccm:1sccm). Subsequently, and without removing the remaining resist, we release the freestanding PCC nanobeam by etching the underlying Si via an isotropic 2 Torr XeF_2 vapor phase process. The resist is not removed prior to optical characterization.

Optical characterization:

All samples were characterized at room temperature using conventional μPL spectroscopy. The attenuated (50 μW) beam of a $\lambda = 514$ nm diode laser was focused to a ~ 1 μm diffraction limited spot by a 40x, NA = 0.6 microscope objective to locally excite the sample. Emission from the sample is collected by the same objective and spectrally analyzed by a 0.5 m grating monochromator equipped with a liquid N_2 cooled Si CCD detector.

Finite Difference Time Domain Simulations:

FDTD simulations were performed using the commercially available software package Lumerical FDTD. We used perfectly-matched-layer absorbing boundary conditions of the simulation region. The PCC was excited by electromagnetic pulses of a wide spectral range around the expected cavity resonance that are emitted by three randomly tilted dipole

sources that are placed in the center of the cavity. The excitation maximum wavelength was slightly detuned from the expected resonance wavelength to avoid overlapping of excitation and emission signal. Time monitors around the cavity center record the time dependent electromagnetic field from 300 fs to 3000 fs after excitation and calculate the emission spectrum by Fourier transformation.

REFERENCES

1. Splendiani, A. *et al.* Emerging photoluminescence in monolayer MoS₂. *Nano Lett.* **10**, 1271–5 (2010).
2. Xu, X., Yao, W., Xiao, D. & Heinz, T. F. Spin and pseudospins in layered transition metal dichalcogenides. *Nat. Phys.* **10**, 343–350 (2014).
3. Zhu, Z., Cheng, Y. & Schwingenschlögl, U. Giant spin-orbit-induced spin splitting in two-dimensional transition-metal dichalcogenide semiconductors. *Phys. Rev. B* **84**, 153402 (2011).
4. Mak, K. F., Lee, C., Hone, J., Shan, J. & Heinz, T. F. Atomically Thin MoS₂ : A New Direct-Gap Semiconductor. *Phys. Rev. Lett.* **105**, 136805 (2010).
5. Wang, Q. H., Kalantar-Zadeh, K., Kis, A., Coleman, J. N. & Strano, M. S. Electronics and optoelectronics of two-dimensional transition metal dichalcogenides. *Nat. Nanotechnol.* **7**, 699–712 (2012).
6. Novoselov, K. S. *et al.* Two-dimensional atomic crystals. *Proc. Natl. Acad. Sci.* **102**, 10451–10453 (2005).
7. Lee, Y.-H. *et al.* Synthesis of large-area MoS₂ atomic layers with chemical vapor deposition. *Adv. Mater.* **24**, 2320–5 (2012).
8. Tao, L. *et al.* Centimeter-Scale CVD Growth of Highly Crystalline Single-Layer MoS₂ Film with Spatial Homogeneity and the Visualization of Grain Boundaries. *ACS Appl. Mater. Interfaces* **9**, 12073–12081 (2017).
9. Klee, V. *et al.* Superlinear Composition-Dependent Photocurrent in CVD-Grown Monolayer MoS₂(1-x)Se_{2x} Alloy Devices. *Nano Lett.* **15**, 2612–2619 (2015).
10. Fu, Q. *et al.* Synthesis and Enhanced Electrochemical Catalytic Performance of Monolayer WS₂(1-x)Se_{2x} with a Tunable Band Gap. *Adv. Mater.* **27**, 4732–4738 (2015).
11. Gan, X. *et al.* Controlling the spontaneous emission rate of monolayer MoS₂ in a photonic crystal nanocavity. *Appl. Phys. Lett.* **103**, 181119 (2013).
12. Wu, S. *et al.* Control of two-dimensional excitonic light emission via photonic crystal. *2D Mater.* **1**, 11001 (2014).
13. Wu, S. *et al.* Monolayer semiconductor nanocavity lasers with ultralow thresholds. *Nature* **520**, 69–72 (2015).
14. Salehzadeh, O., Djavid, M., Tran, N. H., Shih, I. & Mi, Z. Optically Pumped Two-Dimensional MoS₂ Lasers Operating at Room-Temperature. *Nano Lett.* **15**, 5302–6 (2015).
15. Mann, J. *et al.* Facile growth of monolayer MoS₂ film areas on SiO₂. *Eur. Phys. J. B* **86**, 226 (2013).
16. Gong, Y. & Vučković, J. Photonic crystal cavities in silicon dioxide. *Appl. Phys. Lett.* **96**, 31107 (2010).
17. Gong, Y. *et al.* Photoluminescence from silicon dioxide photonic crystal cavities with embedded silicon nanocrystals. *Phys. Rev. B* **81**, 235317 (2010).
18. Rivera, P. *et al.* Observation of long-lived interlayer excitons in monolayer MoSe₂–WSe₂ heterostructures. *Nat. Commun.* **6**, 6242 (2015).
19. Tonndorf, P. *et al.* Single-photon emission from localized excitons in an atomically thin

- semiconductor. *Optica* **2**, 347 (2015).
20. He, Y.-M. *et al.* Single quantum emitters in monolayer semiconductors. *Nat. Nanotechnol.* **10**, 497–502 (2015).
 21. Mak, K. F., He, K., Shan, J. & Heinz, T. F. Control of valley polarization in monolayer MoS₂ by optical helicity. *Nat. Nanotechnol.* **7**, 494–498 (2012).
 22. Zeng, H., Dai, J., Yao, W., Xiao, D. & Cui, X. Valley polarization in MoS₂ monolayers by optical pumping. *Nat. Nanotechnol.* **7**, 490–3 (2012).
 23. Fryett, T. K. *et al.* Silicon photonic crystal cavity enhanced second-harmonic generation from monolayer WSe₂. *2D Mater.* **4**, 15031 (2016).
 24. Rivoire, K., Buckley, S. & Vučković, J. Multiply resonant photonic crystal nanocavities for nonlinear frequency conversion. *Opt. Express* **19**, 22198 (2011).
 25. Notomi, M., Shinya, A., Mitsugi, S., Kuramochi, E. & Ryu, H.-Y. Waveguides, resonators and their coupled elements in photonic crystal slabs. *Opt. Express* **12**, 1551–+ (2004).
 26. Malard, L. M., Alencar, T. V., Barboza, A. P. M., Mak, K. F. & de Paula, A. M. Observation of intense second harmonic generation from MoS₂ atomic crystals. *Phys. Rev. B* **87**, 201401 (2013).
 27. Seyler, K. L. *et al.* Electrical control of second-harmonic generation in a WSe₂ monolayer transistor. *Nat. Nanotechnol.* **10**, 407–11 (2015).
 28. Bao, W., Cai, X., Kim, D., Sridhara, K. & Fuhrer, M. S. High mobility ambipolar MoS₂ field-effect transistors: Substrate and dielectric effects. *Appl. Phys. Lett.* **102**, 42104 (2013).
 29. Lopez-Sanchez, O., Lembke, D., Kayci, M., Radenovic, A. & Kis, A. Ultrasensitive photodetectors based on monolayer MoS₂. *Nat. Nanotechnol.* **8**, 497–501 (2013).
 30. Preciado, E. *et al.* Scalable fabrication of a hybrid field-effect and acousto-electric device by direct growth of monolayer MoS₂/LiNbO₃. *Nat. Commun.* **6**, 8593 (2015).
 31. Pospischil, A., Furchi, M. M. & Mueller, T. Solar-energy conversion and light emission in an atomic monolayer p–n diode. *Nat. Nanotechnol.* **9**, 257–261 (2014).
 32. Sundaram, R. S. *et al.* Electroluminescence in Single Layer MoS₂. *Nano Lett.* **13**, 1416–1421 (2013).
 33. Liu, C.-H. *et al.* Nanocavity Integrated van der Waals Heterostructure Light-Emitting Tunneling Diode. *Nano Lett.* **17**, 200–205 (2017).

ACKNOWLEDGMENTS

This work was funded by Bavaria-California Technology Center (BaCaTeC). S. H., H. M. M. and H. J. K. acknowledge support by Deutsche Forschungsgemeinschaft (DFG) KR3790/2-1 (Emmy Noether Program) and the Cluster of Excellence “Nanosystems Initiative Munich” (NIM). The US National Science Foundation (NSF) supported this work through grant DMR 1609918. Additional support originates from C-SPIN, part of STARnet, a Semiconductor Research Corporation program sponsored by MARCO and DARPA. A.E.N gratefully acknowledge fellowship support under DGE-1326120.

AUTHOR CONTRIBUTIONS

H. J. K. designed research. S. H. fabricated and characterized photonic crystal cavities. S. H. and H.-M. M. developed fabrication process and FDTD modeling. A. E. N., D. M.-T. and S. N. A. performed CVD growth and initial material characterization. S. H., H. J. K. and L. B. wrote the manuscript. H. J. K. and L. B. supervised study.

ADDITIONAL INFORMATION

The authors declare no competing financial interest.